

Hydraulic-mechanical properties of microfaults in granitic rock using the Punch-Through Shear test

Kluge, Christian; Blöcher, Guido; Barnhoorn, Auke; Bruhn, David

DOI

[10.1016/j.ijrmms.2020.104393](https://doi.org/10.1016/j.ijrmms.2020.104393)

Publication date

2020

Document Version

Final published version

Published in

International Journal of Rock Mechanics and Mining Sciences

Citation (APA)

Kluge, C., Blöcher, G., Barnhoorn, A., & Bruhn, D. (2020). Hydraulic-mechanical properties of microfaults in granitic rock using the Punch-Through Shear test. *International Journal of Rock Mechanics and Mining Sciences*, 134, 1-16. Article 104393. <https://doi.org/10.1016/j.ijrmms.2020.104393>

Important note

To cite this publication, please use the final published version (if applicable). Please check the document version above.

Copyright

Other than for strictly personal use, it is not permitted to download, forward or distribute the text or part of it, without the consent of the author(s) and/or copyright holder(s), unless the work is under an open content license such as Creative Commons.

Takedown policy

Please contact us and provide details if you believe this document breaches copyrights. We will remove access to the work immediately and investigate your claim.



Contents lists available at ScienceDirect

International Journal of Rock Mechanics and Mining Sciences

journal homepage: <http://www.elsevier.com/locate/ijmms>

Hydraulic-mechanical properties of microfaults in granitic rock using the Punch-Through Shear test

Christian Kluge^{a,b,*}, Guido Blöcher^{a,c}, Auke Barnhoorn^b, David Bruhn^{a,b}

^a Helmholtz Centre Potsdam - GFZ German Research Centre for Geosciences, Department of Geoenergy, Telegrafenberg, 14473, Potsdam, Germany

^b Department of Geoscience and Engineering, Delft University of Technology, PO-box 5048, 2600 GA, Delft, the Netherlands

^c Institut de Physique du Globe de Strasbourg, UMR 7516, 5 rue René Descartes, 67084, Strasbourg Cedex, France

ARTICLE INFO

Keywords:

Shear fracture
Microfault
Permeability
Aperture
Sustainability
Granite

ABSTRACT

Fault zones are key features in crystalline geothermal reservoirs or in other subsurface environments due to the fact that they act as main fluid pathways. An adequate experimental description of the evolution of permeability of a realistic microscopic fault zone under in-situ reservoir and fracture parallel flow conditions is required. To address this topic, we demonstrate a novel experimental set up (Punch-Through Shear test) that is able to generate a realistic shear zone (microfault) under in-situ reservoir conditions while simultaneously measuring permeability and dilation. Three samples of intact granite from the Odenwald (Upper Rhine Graben) were placed into a MTS 815 tri-axial compression cell, where a self-designed piston assembly punched down the inner cylinder of the sample creating the desired microfault geometry with a given offset. Permeability was measured and fracture dilation was inferred from an LVDT extensometer chain, as well as the balance of fluid volume flowing in and out of the sample. After fracture generation, the shear displacement was increased to 1.2 mm and pore pressure changes of ± 5 or ± 10 MPa were applied cyclically to simulate injection and production scenarios. Formation of a microfault increased the permeability of the granite rock by 2 to almost 3 orders of magnitude. Further shear displacement led to a small increase in permeability by a factor of 1.1 to 4.0, but permeability was reduced by a factor of 2.5 to 4 within 16 h due to compaction and fault healing. Effective pressure cycling led to reversible permeability changes. CT images showed that the fracture network is rather complex, but depicts all features commonly observed in larger scale fault zones.

1. Introduction

The permeability of fractures and faults, or, more generally, shear fractures in crustal rocks has been a substantial research topic in the past. It is not only important in crustal faulting processes or earthquake mechanisms, but is also key in understanding the fluid flow in faulted or enhanced geothermal systems,¹⁻⁴ as well as the stability of underground constructions, such as tunnels or nuclear waste repositories. Fractures control the hydrological and mechanical behaviour of rock masses, such that any changes in fracture properties have a large impact on the bulk transport properties. Laboratory experiments with fractured rock samples are a substantial element to better understand and physically characterise fractures in order to imply physical relationships for the larger scale.

Conventional tri-axial compression tests are classically used to

generate shear fractures or shear zones. Since measuring fracture permeability in such experiments is difficult and fracture permeability cannot be isolated from the rock matrix, other experimental approaches are required. The fractures used for experiments are commonly generated in tensile mode, for example by Brazilian Disk splitting,⁵⁻⁷ or existing, as well as artificial joints are used.⁸⁻¹⁰ The sample halves are then placed together at a certain offset and are installed in a tri-axial cell or shear-box tool to study the permeability evolution. Although the term shear fracture is often applied to such geometries, they do not represent the complex structure of a single shear or fault zone. Several attempts have been made in the past to reproduce a single realistic fault zone in the laboratory. Watanabe et al.¹¹ used a shear-box tool to apply mode II loading to an intact rock sample, but pointed out that it is difficult to generate a single shear fracture from shear-box experiments due to the occurrence of multiple fractures. However, experiments by Frash et al.¹²

* Corresponding author. Helmholtz Centre Potsdam - GFZ German Research Centre for Geosciences, Department of Geoenergy, Telegrafenberg, 14473, Potsdam, Germany.

E-mail address: christian.kluge@gfz-potsdam.de (C. Kluge).

<https://doi.org/10.1016/j.ijmms.2020.104393>

Received 4 June 2019; Received in revised form 17 April 2020; Accepted 15 May 2020

Available online 22 August 2020

1365-1609/© 2020 The Authors. Published by Elsevier Ltd. This is an open access article under the CC BY license (<http://creativecommons.org/licenses/by/4.0/>).

using shale and anhydrite samples highlighted the importance of features, such as en echelon structures, for the aperture anisotropy. Recently, Ye & Ghassemi¹³ used a conventional tri-axial setup with cylindrical double-flawed samples connected to pumps using two injection holes. By increasing the injection pressure, they generated a complex fracture network including shear and tensile fractures and compared the permeability before and after fracture generation.

Besides the challenge to generate a single shear zone while flowing fluid through the sample, permeability is rarely measured during the initiation and propagation of a fracture under in-situ pressure conditions. First attempts to measure permeability while generating a shear fracture in high permeable rocks have been made for example by Zhu et al.¹⁴ or Crawford.¹⁵ De Paola et al.¹⁶ measured the permeability of anhydrite samples during tri-axial testing and subdivided the permeability evolution into three stages of compaction, dilation and brittle failure. Others measured the permeability in tri-axial tests using the pore pressure oscillation method.^{17–19} Mitchell and Faulkner²⁰ quantified the permeability enhancement to about 2 orders of magnitude with the same experimental procedure for granite and granodiorite. However, the shear fractures in these tests were not parallel to the flow direction or the entire sample integrity was lost during failure, which makes it difficult to isolate the mechanical and hydraulic behaviour of the fracture from the surrounding rock mass. Watanabe et al.¹¹ fractured granite samples in a shear-box tool and measured the permeability of these samples in another flow-through apparatus. Although a flow parallel fracture geometry is given, no fluid flow was applied during fracturing and the sample had to be removed from the shear apparatus after fracture generation, which highly alters the hydraulic-mechanical fracture properties.

The permeability during shearing is substantial for the understanding of the processes involved in hydro-shearing or the permeability evolution in active faults. In some experimental studies, asymmetric loading conditions on a pre-existing tensile fracture in cylindrical samples with different end cap designs were used to displace a fracture while measuring permeability.^{17,21,22} Shear-box tools were also used to displace a fracture under normal loading conditions,^{23,24} but the normal effective pressures in these tests were too low to make meaningful conclusions or additional fractures formed. Watanabe et al.¹¹ compared the permeability of displaced tensile fractures and fractures generated by shearing and found that displaced tensile fractures have a higher permeability and a higher resistance to closing compared to shear fractures when increasing normal stress. More frequently, tri-axial set ups with injection-holes are used to generate a shear displacement on a pre-existing planar shear plane in different materials.^{25,26} Other authors performed stick-slip experiments with artificial surfaces,^{27,28} which are sheared while measuring permeability. Although it is possible to accurately quantify permeability, the experimental set ups mentioned involve unrealistic planar fracture surfaces, which lead to only marginal permeability changes or are performed at very low normal stress.

The longevity or sustainability of the generated permeability enhancement by fracturing is crucial for engineering applications, in which, for example, pore pressures change due to production and injection schemes, or the fracture aperture changes due to stress relaxation when the well is not operated. In experimental studies with granite,^{5,11,29,30} the effective pressure was varied by changing the confining pressure cyclically using displaced tensile fractures in granite and found a progressive reduction in permeability with each cycle. However, manually displaced tensile fractures might have a different initial strength during the first loading stages compared to faults. Furthermore, a variation in confining pressure is different compared to changing the pore pressure when considering effective pressure coefficients.³¹ Zangerl et al.³² evaluated the fracture normal stiffness of several granite samples and provided a range of values, without finding systematic changes, but highlighted the importance of surface geometry and asperity deformability. Lastly, permeability losses are often observed in experiments and are related to mechanical compaction^{17,27}

or fluid-rock interactions.³³ Therefore, effective pressure cycling, fracture stiffness characterisation, as well as compaction induced permeability reductions need to be considered for complex shear fracture or fault geometries. There is too little quantification of permeability enhancement in granite during shear fracture generation or permeability evolution during shearing and only a few of those studies account for a realistic shear zone geometry, or they are limited in terms of the displacement magnitude.

We present an approach to combine most of the above-mentioned experimental technologies in a single experiment. The evolution of permeability during initiation and propagation of a circular shear fracture (referred to as a microfault in the following) is presented, using the Punch-Through-Shear (PTS) test, originally developed to measure mode II fracture toughness.^{34–38} The existing experimental setup has been supplemented with the possibility of saturating the sample and allowing fluid flow-through to measure the pressure gradient across the sample. This enables us to determine the permeability of an artificially-generated microfault with flow oriented parallel to the fracture. The PTS test allows for the quantification of the permeability during fracture initiation, propagation and effective pressure changes, an analysis of fracture properties and geometry, as well as an assessment of its hydraulic-mechanical sustainability.

2. Materials & methods

2.1. Testing equipment

The Punch-Through-Shear (PTS) test was carried out in a conventional MTS tri-axial compression cell. The stiff, servo-controlled loading frame (MTS 815, Material Testing Systems Corporation) holds a loading capacity of up to 4600 kN (load cell calibrated to 1000 kN, calibration error < 1%) and a servo-controlled maximum hydrostatic confining pressure of 140 MPa applied via an oil-filled pressure vessel coupled to an external pressure intensifier. The pore fluid pressure was applied via four Quizix fluid pressure pumps (Model C6000-10K-HC-AT) with a maximum fluid pressure of 70 MPa. Flow-through was continuously applied at a minimum of 2 MPa confining pressure using two paired upstream pumps and two paired downstream pumps. The differential fluid pressure, which is the difference between in- and outflow pressure, was measured using a differential pressure sensor (Honeywell HL-Z; range: 1 MPa; line pressure max. 35 MPa; precision: ~1%). Changes in circumferential strain were measured using a LVDT extensometer chain. All experiments have been performed at ambient conditions, i.e. temperatures of 25–30 °C. Data were recorded at a frequency of 1 Hz. A detailed description of the machine is found in Pei et al.³⁹

2.2. Sample material

The testing material is a granite from the Odenwald region ([International Geo Sample Number \(IGSN\): GFTRE0033](#)) taken from a quarry in Rimbach, Germany. The fresh granite shows no signs of strong alterations or microfracturing (Fig. 1c–f). It is composed of quartz (Qtz) with a grain size ranging from 1 to 3 mm, feldspar (Fsp) between 2 to 3 mm and mica (Mca) between 1 to 3 mm, suggesting a very even size distribution of minerals. Quartz, as well as the darker and brighter mica are the main constituents, feldspars have a less frequent occurrence. Microfractures are only partially present and either cut through grains, or propagate along grain boundaries with no visible shear offset. The porosity of less than 0.6% is mostly intra-granular and rarely connected. The intact rock properties of the Odenwald granite, in the following labelled as PGR6-RI,⁴⁰ are summarized in Table 1. Three granite samples have been tested with their testing conditions and sample dimensions listed in Table 2.

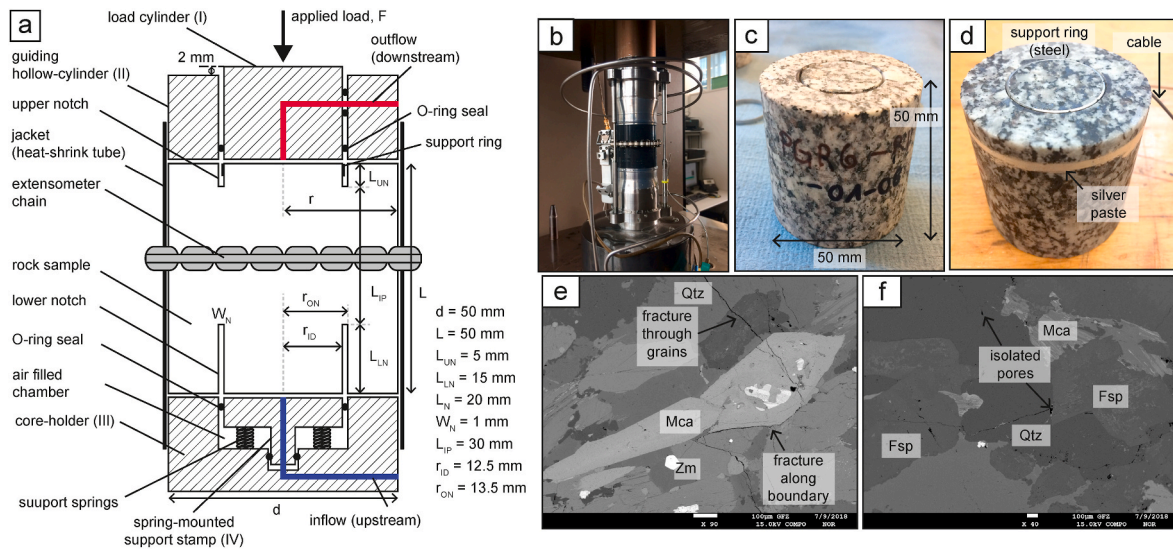


Fig. 1. a) Experimental set up and dimensions, b) Experimental set up, c) Odenwald granite sample (PGR6-RI), d) integrity test, e) and f) electron probe micro-analyser (EPMA) images of the intact rock.

Table 1
Intact rock properties of samples PGR6-RI according to Blöcher et al.⁴⁰

| | TS [MPa] | K_{IC} [MPa·m ^{0.5}] | UCS [MPa] | E [GPa] | ν [-] | ϕ [%] | k_{ini} [m ²] |
|-----------------|----------|----------------------------------|-----------|--------------|--------------|------------|-----------------------------|
| IGSN: GFTRE0033 | 11.8 | 1.347 | 120–142 | 39.9 to 47.6 | 0.19 to 0.26 | >0.5 | >10 ⁻¹⁸ |

TS: tensile strength, K_{IC} : mode I fracture toughness, UCS: uniaxial compressive strength, E: Young’s modulus, ν : Poisson ratio, ϕ : porosity, k_{ini} : initial permeability.

Table 2
List of samples, sample dimensions and testing conditions.

| Sample ID | Testing conditions | L_{IP} [mm], L [mm], d [mm] | Additional measurements | Comments |
|---------------|--|-------------------------------|---|--|
| PGR6-RI-01-07 | Failure: $P_c = 40$ MPa, $P_p = 20$ MPa; Pressure cycling: none | 31.40, 49.4, 50.05 | Integrity of electrical circuit of silver paste, no LVDT extensometer chain | Small leak at the outlet, no reliable fluid volume data without impact on permeability |
| PGR6-RI-01-08 | Failure: $P_c = 40$ MPa, $P_p = 20$ MPa; Pressure cycling: 5 MPa | 30.15, 50.15, 50.10 | LVDT extensometer chain, x-ray CT scanning | |
| PGR6-RI-01-09 | Failure: $P_c = 40$ MPa, $P_p = 20$ MPa; Pressure cycling: 10 MPa | 30.18, 50.19, 50.10 | LVDT extensometer chain, x-ray CT scanning | |

P_c : confining pressure, P_p : pore pressure, L_{IP} : length of intact portion, L: sample length, d: sample diameter.

2.3. Sample geometry & experimental setup

The idea of the Punch-Through-Shear (PTS) test is to have a notched intact cylindrical sample, of which a smaller inner part (inner cylinder) is punched through the surrounding hollow cylinder. The main objective is to generate a shear stress concentration at the notch tips generating a circular shear fracture (microfault) connecting the bottom and top notch of a cylindrical rock sample. The experimental set up and sample geometry are illustrated in Fig. 1a and b.

The set up consists of a piston assembly that applies a load to the top inner cylinder and the bottom outer annulus of the sample, as well as a core-holder system supporting the sample at the bottom, both made of stainless steel. The cylindrical samples were drilled from larger blocks to a diameter, d , of 50 mm using a diamond drill bit and water as lubricant. The samples were cut to length, L , of 50 mm using a diamond saw, and the end-surfaces were ground plan-parallel. The notches were then drilled using a diamond drill bit with an inner diameter, r_{ID} , of 25 mm

and a wall thickness, i.e. notch width, W_N , of 1 mm. Top notch depth and lower notch depth were 5 and 15 mm respectively, resulting in an intact portion, L_{IP} , of 30 mm. This intact portion, L_{IP} , was larger compared to the 15 mm suggested by the ISRM International Society for Rock Mechanics and Rock Engineering,³⁵ but was used to enable the proper characterisation of the hydraulic, mechanical and geometrical properties of the microfault. This deviation from the recommended design is acceptable, as no variations in fracture toughness up to a length of 35 mm were previously found.^{35,37,38} The mechanical integrity of the top-notch walls was supported by a 0.3 mm strong steel ring (2 mm shorter than the top notch length L_{UN}) to prevent breakouts and compaction that were observed in pre-tests without a supporting ring (Fig. 1d). Due to its shorter length the ring is assumed to not cause axial stress to the rock sample itself. The sample was covered with a heat-shrink tube to prevent confining fluid from entering the sample.

The loading assembly, shown in Fig. 1a, consists of a mobile steel cylinder of 25 mm in diameter (I), guided by a surrounding hollow

cylinder (II), which is 2 mm shorter than the mobile inner cylinder. The space in between the two parts is sealed by O-rings to prevent oil from entering the sample. The lower part of the assembly consists of a rigid core-holder system with a hollow cylindrical shape to counteract the applied load from the top (III). A movable smaller core-holder in the middle (IV), also sealed with O-rings, is mounted on a set of springs in an air-filled chamber. This is to prevent the inner cylinder from falling down instantly after failure and allows for a controlled displacement along the fracture. Fluid ports were incorporated within the loading assembly and core-holder system, sealed from the confining fluid by O-rings. A grid across the surface of the end caps allows for uniform in- and outflow across the entire cross-sectional area (top and bottom) of the sample. An extensometer chain (LVDT) attached at the centre between upper and lower notch is used to record the bulk circumferential strain throughout the entire duration of the test. Furthermore, the integrity of the sample wall during one experiment was monitored (PGR6-RI-01-07). Silver paste was applied to the circumference of the sample connected to an electronic circuit, such that any fracturing of the wall would result in an interruption of the electric signal (Fig. 1d).

2.4. Experimental procedures

The sample was installed in the measuring assembly and an absolute pore pressure of 10 mbar was generated using a vacuum pump (Laboxact SEM 820). The confining pressure was increased from 0 to 2 MPa at a rate of 0.5 MPa/min with the dry sample. After applying the vacuum, the system was saturated by applying a constant fluid pressure of 0.2 MPa from the upstream side. That way, water flew into the sample under nearly vacuum conditions, such that all pores were saturated. Saturation was finished when no more water flew into the sample to avoid effects of the saturation process to govern the permeability at later stages of the experiments.⁵ For all permeability measurements, a constant flow rate (0.4–1 ml/min) was applied to the bottom of the sample and a constant pressure was applied at the downstream side (10–30 MPa) to determine the sample permeability. Steady-state conditions were reached when the flow rates and pressure difference reach a constant value. Sample permeability, k , was calculated by equation (1) using Darcy's law,⁴¹ where the length, L_{IP} , is the distance between the lower and upper notch which corresponds to the maximum pressure gradient in the microfault. The sample permeability, k , corresponds to the permeability of the rock portion between the notches, assuming there is no pressure gradient along the 1 mm wide notches:

$$k = (Q/A) * (\mu L_{IP}) / dP \quad (1)$$

where Q is the volumetric inflow rate in m^3/s , A is the cross-sectional area of the sample in m^2 , μ is the dynamic viscosity of the fluid (Pa s), L_{IP} is the distance between the notches of the sample in m and dP is the differential fluid pressure in Pa. The minimum measurable permeability of our apparatus is around $k = 10^{-18} m^2$. It is important to note, that steady-state permeability, k_{ss} , was measured during the hold phase (C), during shearing (D) and before pressure cycling (E), as well as during the constant pressure phases during cyclic loading (F). In contrast, flow conditions were transient, k_{trans} , during the fracturing process (B) and during pore pressure ramping (F). These measurements were labelled as apparent permeability in the results, although they were calculated using equation (1). Comparing the minimum measurable permeability and the permeability after the hold phase, the fold of increase in permeability, $k_{FOI} = k_{ss}/k_{hold}/10^{-18}$, was calculated to infer the permeability enhancement by fracturing.

During the fracturing process, an elevated effective pressure state is desired, where Terzaghi's effective pressure,⁴² P_{eff} (equation (2.1)), is defined as the confining pressure, P_c , minus fluid pressure, P_p . The pore fluid pressure was estimated by the outflow pressure, $P_{p,out}$, and the differential fluid pressure, $P_{p,in} - P_{p,out}$, divided by two (equation (2.2)), assuming a linear pressure distribution^{5,6}:

$$P_{eff} = P_c - P_p \quad (2.1)$$

$$P_p = P_{p,out} + (P_{p,in} - P_{p,out})/2 \quad (2.2)$$

The change of volume of fluid in the sample, V_b (bulk volume) was determined according to equation (3) from the difference of cumulative inflow (V_{in}) and cumulative outflow volume (V_{out}) in ml:

$$V_b = V_{in} - V_{out} \quad (3)$$

After saturating the sample at 2 MPa confining pressure, the fluid pressure and confining pressure were simultaneously increased to 20 MPa and 40 MPa, respectively, within 1 h to an effective pressure of 20 MPa (Fig. 2, A). Afterwards, an axial displacement rate of 0.001 mm/s was applied to the top of sample (Fig. 2, B), which pushed the inner loading cylinder down relative to the guiding hollow cylinder until the point of failure. A drop in axial load, F , indicated the formation of a fracture. Up to this point, the inflow and outflow pressure were kept constant at a differential fluid pressure of 0.5 MPa. The fracture geometry was intended to initiate from the outer lower notch tip to the inner upper notch tip,³⁵ resulting in an overall conical shape.

The mode II fracture toughness, K_{IIc} , or critical stress intensity factor, is a material parameter obtained by the PTS test, and depends on the type of rock material and its physical boundary conditions, such as confining pressure and temperature.^{36,37} The fracture toughness (K_{IIc}) was calculated at the point of failure by the following empirical relation (equation (4)) based on the ISRM Suggested Methods³⁵:

$$K_{IIc} = 7.74 * 10^{-2} F_{max} - 1.80 * 10^{-3} P_{eff} * 10^{-3} \quad (4)$$

where F_{max} is the peak load in kN and P_{eff} is the effective pressure in MPa. Using the circumferential extensometer, the mechanical fracture dilation (e_{mech}) can be calculated by converting the change in circumference (dU) in mm to a change in radius:

$$e_{mech} = dU/2\pi \quad (5)$$

The fracture dilation is assumed to approximate the fracture aperture during the test. In addition, the changes in volume (equation (3)) were used to calculate the volume balance-based dilation e_{vol} . This was only possible during phase B, since the change of cumulative fluid volume could be measured when a constant differential fluid pressure was applied. During fracture generation, additional void is generated. This is composed by the opening of the fracture itself, as well as the widening of the notches. The widening of the two notches is considered at the outer notch radius, r_{ON} . The additional volume can then be approximated as follows:

$$\Delta V_{notch} = \Delta e 2r_{ON} \pi L_N \quad (6.1)$$

where r_{ON} is the radius to the outer notch, L_N is the total length of the upper and lower notch and e is the dilation with all units in m. The fracture has a shape of a truncated cone with a mantle surface area of $(r_{ON} + r_{ID}) \pi L_{frac}$. Here, L_{frac} is the fracture length measured from the lower outer and top inner notch, r_{ID} is the inner radius and r_{ON} the radius to the outer notch wall (Fig. 6c). The additional volume due to fracture generation can then be calculated as follows:

$$\Delta V_{frac} = \Delta e (r_{ON} + r_{ID}) \pi L_{frac} \quad (6.2)$$

The total volume change measured $\Delta V_{measured} = \Delta V_{notch} + \Delta V_{frac}$, can be used to estimate the fracture dilation, e_{vol} :

$$e_{vol} = V_{bulk} / ((2r_{ON} \pi L_N + (r_{ON} + r_{ID}) \pi L_{frac}) \quad (6.3)$$

After failure, the axial displacement ramp was stopped (hold phase) and the constant pressure boundaries for the fluid flow were changed to a constant inflow rate and a constant downstream pressure until a constant differential pressure of at least 0.1 MPa was reached and permeability was measured (Fig. 2, C). After that, the axial displacement

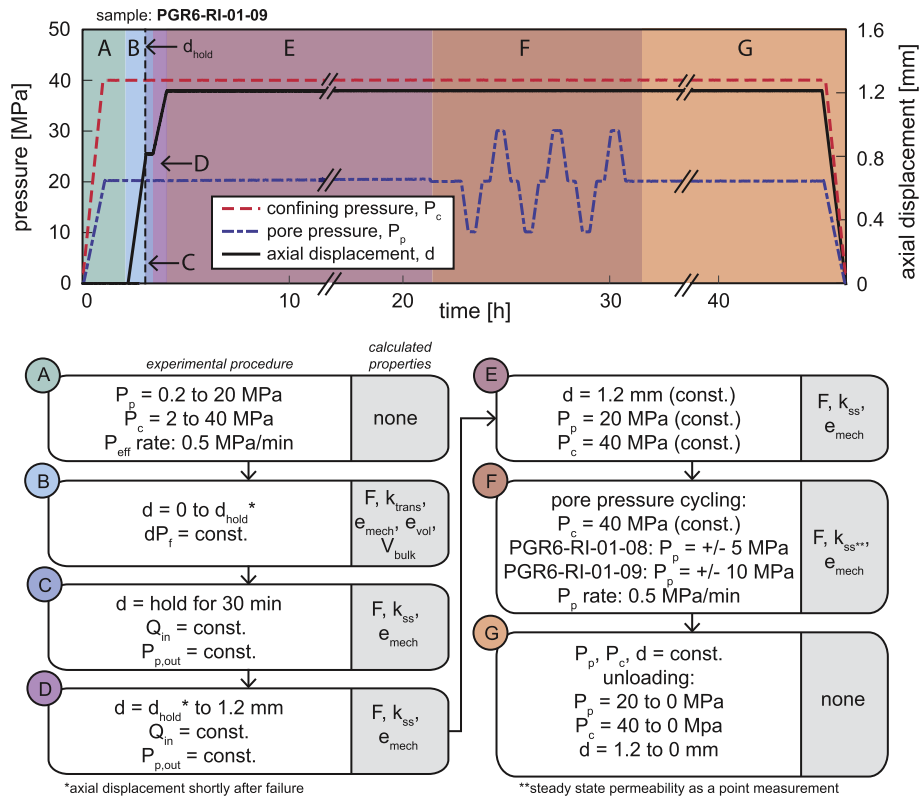


Fig. 2. Experimental procedure and flow chart of the respective phases (A–G).

was again increased at a slower rate of 0.0001 mm/s leading to an increase in shear displacement until a maximum of around 1.2 mm was reached (Fig. 2, D). Finally, the axial displacement of the loading cylinder at the top was maintained to measure changes in stress and was kept in this position for at least 16 h (Fig. 2, E).

After that, the effective pressure was varied cyclically by changing the mean fluid pressure in the sample by ± 5 or ± 10 MPa (Fig. 2, F). A constant ramp operation of fluid pressure (0.5 MPa/min) was applied to the outflow side of the sample with the inflow pressure following the given ambient pressure change without active operation. Steady state flow conditions were achieved when the inflow and outflow pressure and rates reached a constant value, which took about 10 min considering a hydraulic diffusivity of about $4.5 \cdot 10^{-6}$ m²/s for a length of 0.05 m calculated according to Nicholas et al.⁴³ For the diffusivity we used a conservative matrix permeability of $1 \cdot 10^{-19}$ m², Biot and Skempton coefficients of 0.4 and 0.6 and a bulk compressibility of 30 GPa reported for granite.⁴⁴ During pressure cycling, the vertical load, F , was transformed into shear stress,³⁵ τ using equation (7):

$$\tau = F / (\pi r_{ID} L_{frac}) \quad (7)$$

where r_{ID} is the inner diameter in m and L_{frac} is the fracture length in m. This equation assumes and simplifies that the fracture to be a single plane. The fracture stiffness describes the fracture closure behaviour under increasing effective normal pressure. For a semi-logarithmic closure law⁴⁵ only one free parameter, the fracture stiffness characteristic, χ , is required and was obtained from the slope of the effective normal pressure versus fracture aperture change^{32,46} following equation (8):

$$\ln(P_{eff}) = \chi \Delta e_{mech} + \ln(\sigma_n^{ref}) \quad (8)$$

P_{eff} is the normal effective pressure in MPa, χ , the fracture stiffness characteristic in mm⁻¹, Δe_{mech} is the change in mechanical dilation in mm and σ_n^{ref} is any arbitrary reference value of normal stress in MPa.

After effective pressure cycling was finished, the testing conditions were kept constant for another 12 h, until the axial displacement, fluid and confining pressure were decreased simultaneously at similar rates as at the loading stage (Fig. 2, G).

3. Experimental results

In the following, the process of microfault generation and propagation is described and the results for permeability evolution, flow rate changes, fracture dilation and volume balance during loading are given (Figs. 3–5). The evolution of shear stress, dilation, permeability and fracture stiffness for cyclic effective pressure loading are also presented (Figs. 7–9). Furthermore, the fracture geometry is described using the computed x-ray CT imaging (Fig. 10). The overall results are summarized in Table 3.

3.1. Fracture generation

The loading and failure process can be subdivided into five regimes with different dominant processes (Figs. 3–5). The stages of fracture initiation and propagation are illustrated in Fig. 6.

During stiffening and compaction at the first stage of loading, the volume of the sample was reduced and water was squeezed out of the sample. Between 0.60 to 0.65 mm of axial displacement, the inflow rate started to increase, the load curve flattened and the volume balance reached an inflection point (Fig. 3a and b; 4a, b, c and 5a, b, c). At this point, fracture initiation took place from the bottom of the sample, indicated by an increased inflow rate and a misbalance between in- and outflow, leading to dilation and a consequent increase of fracture volume of the sample (Fig. 6). Using equations (5) and (6.3), the mechanical fracture dilation and the volume balance-based dilation was calculated, respectively, since it was assumed that a fracture is introduced into the sample. The mechanical dilation, which represents the change in mechanical aperture, increased faster than the volume-based

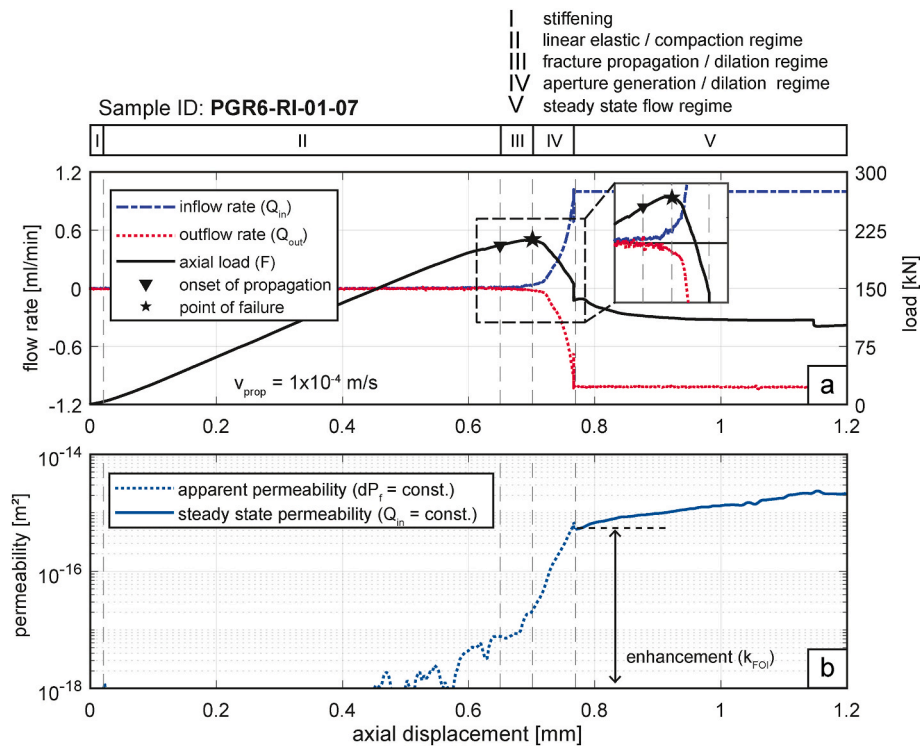


Fig. 3. The change in inflow and outflow rate and axial load vs. the axial displaced (a) and sample permeability during fracturing and shearing (b).

dilation, since it took longer for the pore fluid to progress through the sample and the circumferential strain was only measured at the centre of the intact portion.

At the point of failure, the axial load reached values of about 212, 203 and 197 kN which is equal to 424, 406 and 394 MPa axial stress, which corresponds to 384, 366 and 354 MPa differential stress for sample PGR6-RI-01-07, PGR6-RI-01-08 and PGR6-RI-01-09, respectively. The load then dropped and the increase in outflow rate indicated a hydraulic short-cut between the lower and upper notch, suggesting a fully developed fracture system. Calculating the mean fracture propagation velocity, v_{prop} , which is simply the length of the fracture, L_{frac} , over the time span of fracture initiation to the point of failure, t_{prop} , the velocity was in the range of 0.1–0.3 mm/s ($v_{prop} = L_{frac} / t_{prop}$). After failure, at a displacement of about 0.7–0.8 mm, the inner cylinder was punched down and most of the aperture was created, indicated by a rapid increase in mechanical and volume-based dilation. The measured load was now controlled by the frictional properties of the fracture. Shortly after the point of failure the displacement was put on hold for about 30 min (hold phase) such that the fluid pressure field could reach steady state flow conditions. The final value for dilation and fracture volume were reached during the hold phase when fluid pressure diffusion was finished. After restarting the displacement up to a maximum of 1.2 mm all samples showed no drop or rapid increase in axial load, i.e. no “stick slip” behaviour, but rather approached a limiting value of about 75 and 100 kN. This behaviour of fracture generation and propagation was similar in all three experiments. The fracture toughness values (equation (4)) for the saturated granite samples ranged between 15.3 and 16.4 $\text{MPa} \cdot \text{m}^{0.5}$ (Table 3).

3.2. Permeability and dilation evolution during failure

During all tests, the permeability was measured simultaneously during loading and failure. The flow conditions during failure were regarded as transient (apparent permeability, k_{trans}), but steady state after the hold phase (steady-state permeability, k_{ss}). The permeability evolution during fracture generation is shown in Figs. 3b, 4d and 5d,

where all experiments showed a pre-failure increase in apparent permeability of half to almost one order of magnitude, coinciding roughly with the inflection point of the volume balance as well as with the onset of yielding. For all granite samples, the increase in permeability was about 2 to almost 3 orders of magnitude at an effective pressure of 20 MPa ($P_c = 40$ MPa, $P_p = 20$ MPa), comparing the pre-failure permeability and the permeability during the hold phase (k_{FOI} , Table 3). As explained before, the main dilation and consequent permeability was generated after the point of failure, with values of 0.06–0.07 mm (PGR6-RI-01-08) and 0.07–0.08 mm (PGR6-RI-01-09), while mechanical dilation and volume-based dilation were in very good agreement, suggesting that the measured dilation corresponds to the mechanical aperture. After the hold phase, the microfault was displaced up to 1.2 mm, resulting in a gentle increase in mechanical dilation to about 0.1 mm for sample PGR6-RI-01-08 and 0.09 mm in sample PGR6-RI-01-09, while permeability was consequently relatively constant. The maximum additional increase was between a factor of 4.0 for sample PGR6-RI-01-07 and 1.1 for sample PGR6-RI-01-09. No additional fracturing was inferred from the mechanical-hydraulic and electrical data (PGR6-RI-01-07) during this period. Permeability decay curves measured for about 16 h were similar for two granite samples at 20 MPa effective pressure and showed a reduction by a factor of 2.5 to 4 (inset Figs. 4d and 5d).

3.3. Permeability evolution during pore pressure cycling

To simulate reservoir operation procedures, such as injection or production, the pore pressure was cycled in two samples in order to monitor possible changes in shear stress due to slipping of the fault, permeability and strain at varying effective pressure (Figs. 7 and 8). The starting pore pressure of 20 MPa was varied by ± 5 MPa (PGR6-RI-01-08) and ± 10 MPa (PGR6-RI-01-09), corresponding to a change of around 500–1000 m in the water column in a geothermal well. In total, six cycles of pore pressure increase and decrease were performed for each experiment.

The permeability was reduced when the pore pressure was reduced

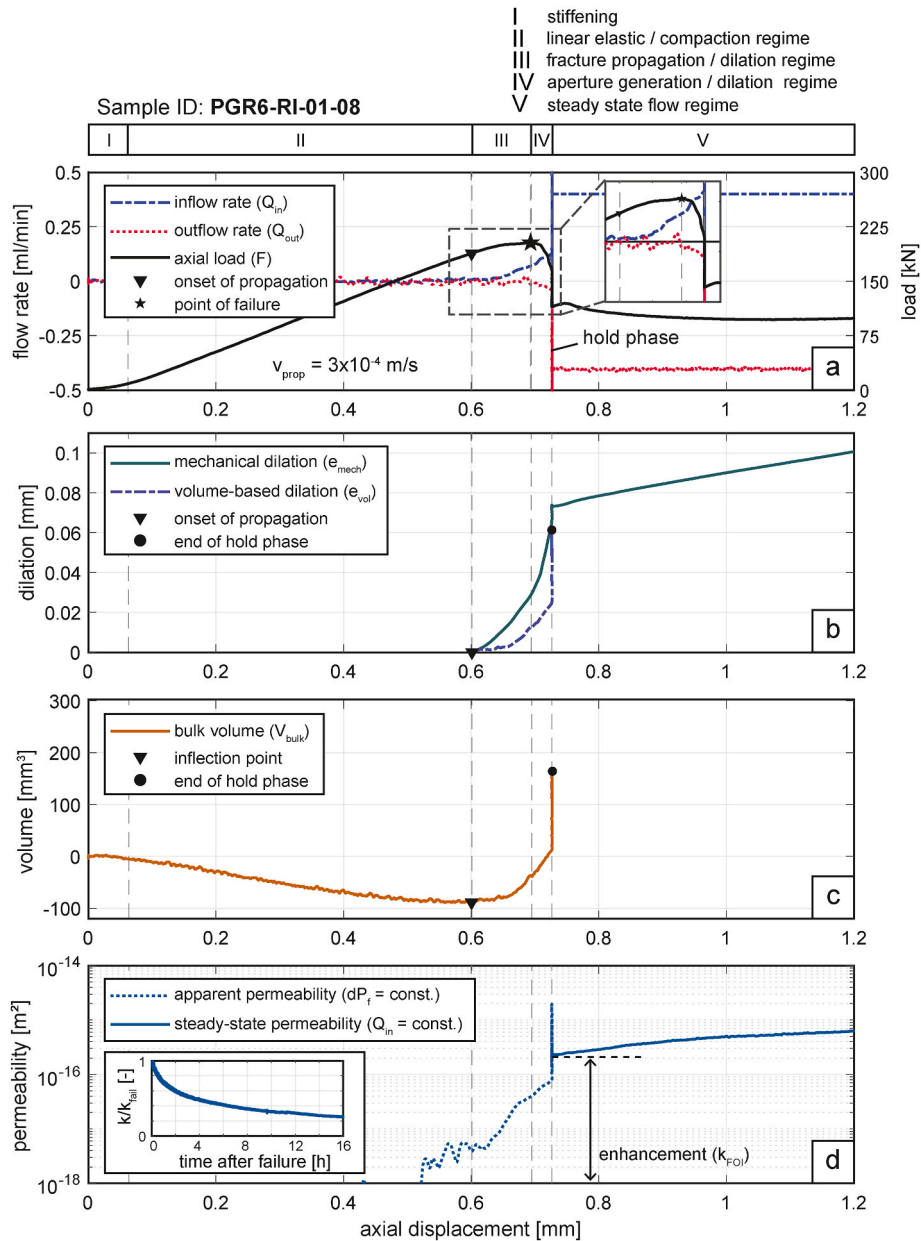


Fig. 4. The change in inflow and outflow rate and axial load vs. the axial displaced (a), mechanical and volume-based aperture (b), fracture volume (c) and sample permeability (d).

(effective pressure increase), while the permeability increased for increasing pore pressure (effective pressure decrease). The total variations in permeability for the pressure changes of ± 5 MPa (PGR6-RI-01-08, Fig. 7b) ranged from $8.53 \times 10^{-17} \text{ m}^2$ to $2.57 \times 10^{-16} \text{ m}^2$, while permeability varied from $3.84 \times 10^{-16} \text{ m}^2$ to $6.0 \times 10^{-17} \text{ m}^2$ for pressure variations of ± 10 MPa (PGR6-RI-01-09, Fig. 8b). Permeability was slightly increased from $1.10 \times 10^{-16} \text{ m}^2$ to $1.58 \times 10^{-16} \text{ m}^2$ after six pressure cycles for the variations of 5 MPa (PGR6-RI-01-08). Similar, a minor permanent increase from $8.65 \times 10^{-17} \text{ m}^2$ to $1.17 \times 10^{-16} \text{ m}^2$ was observed for the effective pressure variations of 10 MPa (PGR6-RI-01-09). Comparing the mechanical dilation evolution (Figs. 7c and 8c), both samples showed a similar behaviour, which is opening during the pore pressure increase (effective pressure decrease) and closure during the pore pressure decrease (effective pressure increase). Doubling the pore pressure change led to a doubling in magnitude of the dilation change.

During the pore pressure changes, the load cylinder was maintained at a constant vertical position after the maximum displacement was

reached. This way, the shear stress evolution was obtained from the measured vertical load (equation (7), Figs. 7a and 8a). When the pore pressure is varied, the effective normal stress is also changed, which can lead to slip events when a failure criterion is exceeded, resulting in a change in shear stress. For the 5 MPa effective pressure variation, a reduction in shear stress (“slip event”) was observed in the 5th and 6th cycle, reducing the shear stress by about 5 MPa. For the 10 MPa effective pressure variation the decrease in shear stress occurred in the 2nd cycle already with a larger magnitude of reduction of about 10 MPa. The vertical stress in the system could only be released towards the bottom of the sample, where the core of the sample was mounted on springs (top load piston was fixed). Since the dilation change suggested only small changes in lateral direction (Figs. 7c and 8c), we assume that this stress release resulted in a downward movement of the inner cylinder, such as a “slip event”, i.e. a small vertical displacement along the microfault. The friction coefficient could not be calculated since the normal stress was possibly disturbed by the sample and fracture geometry and needed

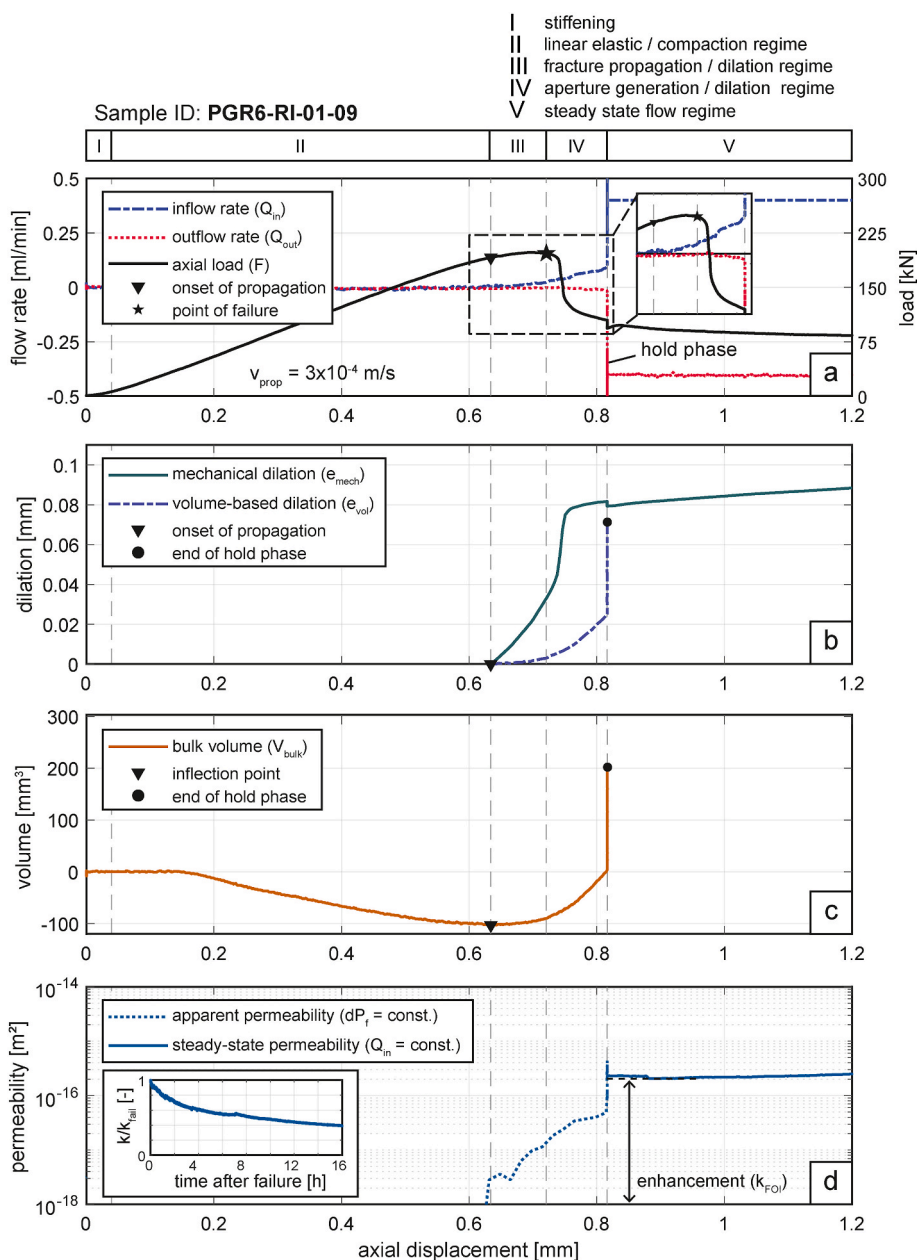


Fig. 5. The change in inflow and outflow rate and axial load vs. the axial displaced (a), mechanical and volume-based aperture (b), fracture volume (c), sample permeability (d).

to be determined numerically. The slip events resulted in a small reduction of permeability for a change of 5 MPa in pore pressure, accompanied by further fracture closure. Conversely, the slip event for the 10 MPa pore pressure change resulted in a slight increase in permeability and a dilation increase. However, the mechanical dilation was only measured at the centre of the intact portion (L_{IP}), such that opening or closing during slip depends on the orientation of the fracture at this location.

The fracture stiffness, χ , was obtained at each loading cycle during pore pressure reduction (equation (8)). It was observed that the fracture stiffness increases with each loading cycle and that fractures stiffness was higher when the initial effective pressure level was higher (Fig. 9), while the permeability was not significantly changing with an increasing number of pressure cycles. Generally, the permeability changes and fracture stiffness suggested a mechanically and hydraulically sustainable fracture.

3.4. Fracture geometry from x-ray micro-CT scan analysis

Computed x-ray CT scanning was performed using the entire sample after testing to visualize the deformation within the sample. We used a nanotom® ultra-high resolution nanoCT system with a 360° scanning projection, providing a resolution for our sample size (50 by 50 mm) of about 25 μ m. Computed x-ray CT scanning images of the microfaults in samples PRG6-RI-01-08 and PGR6-RI-01-09 revealed a complex micro-fault zone connecting the upper and lower notch of the sample (Fig. 10). The major fault zone was characterised by step-over structures, clearly displaced fracture faces with a visible self-propping effect, fracture branching, as well as particles or breccia distributed across the shear zone. Radial fractures and horizontal fractures were secondary features that formed during the unloading to atmospheric pressure at the end of the test and therefore do not contribute to permeability. They usually terminate against fracture branches of the central shear zone and are found in areas where the two fracture faces are in contact, thus

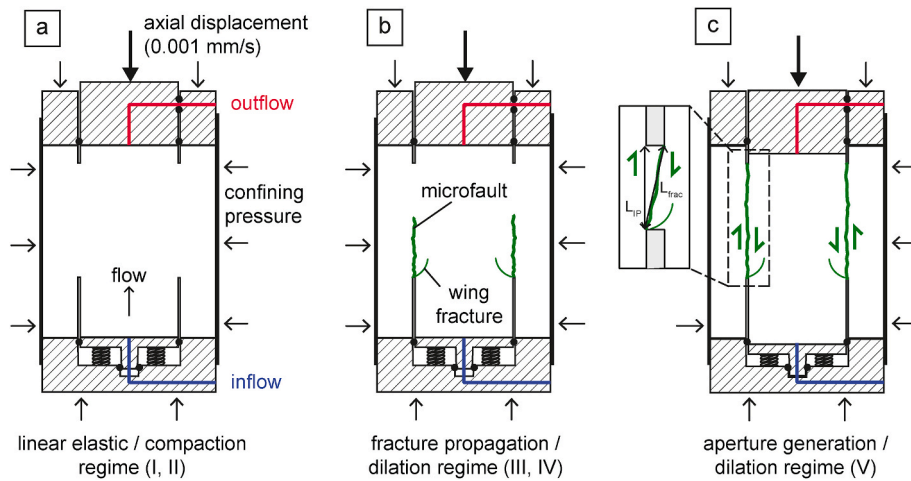


Fig. 6. Illustration of the fracture propagation process during the different stages: a) linear elastic phase, b) fracture propagation, c) shear displacement along a principal shear plane.

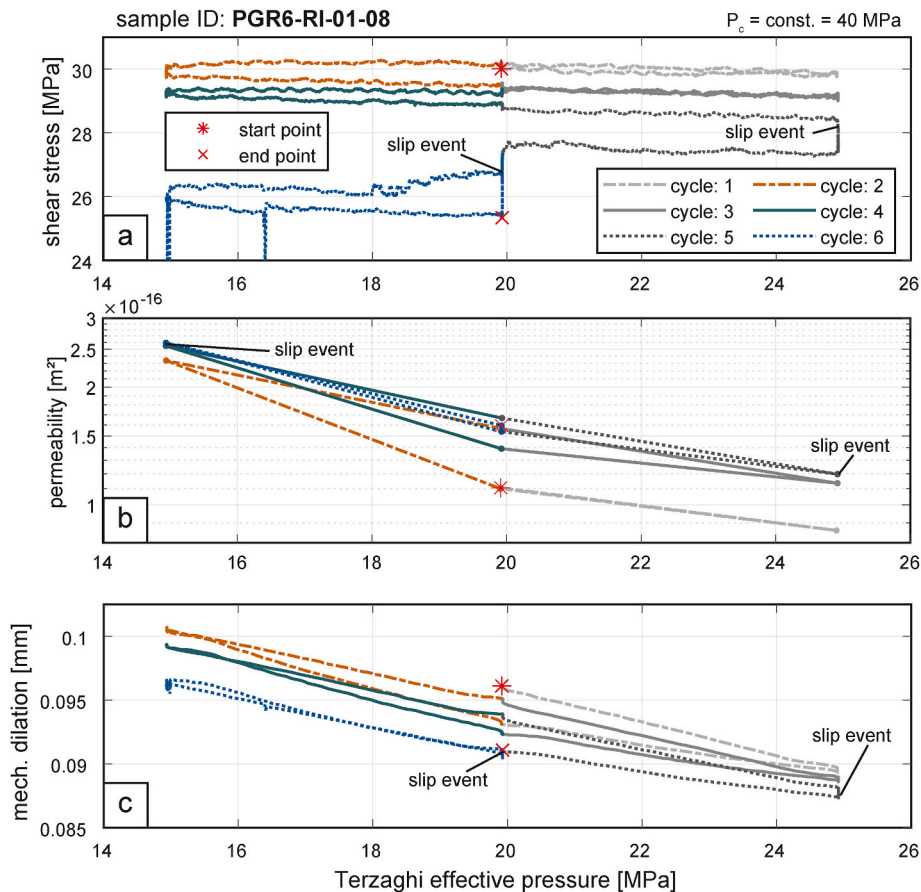


Fig. 7. Shear stress (a), permeability (b) and mechanical aperture (c) evolution during effective pressure changes of 5 MPa (sample PGR6-RI-01-08).

minimising permeability.

True apertures were measured at defined distances of about 0.5–0.8 mm along the fracture in x-y oriented cross sections at different height levels (21 levels with about 2300 measured apertures, N , for each sample) between the bottom and top notch (Fig. 10). Closed sections (apertures smaller 0.01 mm), as well as open sections were measured in order to obtain a contact-area ratio, R_c , which was defined as the amount of contact points (zero aperture) over the total number of measurements, N . Based on the aperture distribution, mean aperture, contact area ratio

and the structural features of specific areas along the vertical fracture, three specific zones were identified (zone I, II and III).

For sample PGR6-RI-01-08, zone I showed mostly apertures between 0.05 and 0.2 mm with mean apertures indicated in Fig. 10. The top part of the fracture was highly damaged and crushed. Below, a zone of transpressional features was visible with a mean aperture of 0.087 and a contact area ratio of 20% indicated as zone I. Zone II was characterised by almost vertically oriented fractures (simple shear zone) showing the highest contact area ratio of about 34% and a mean aperture of 0.089

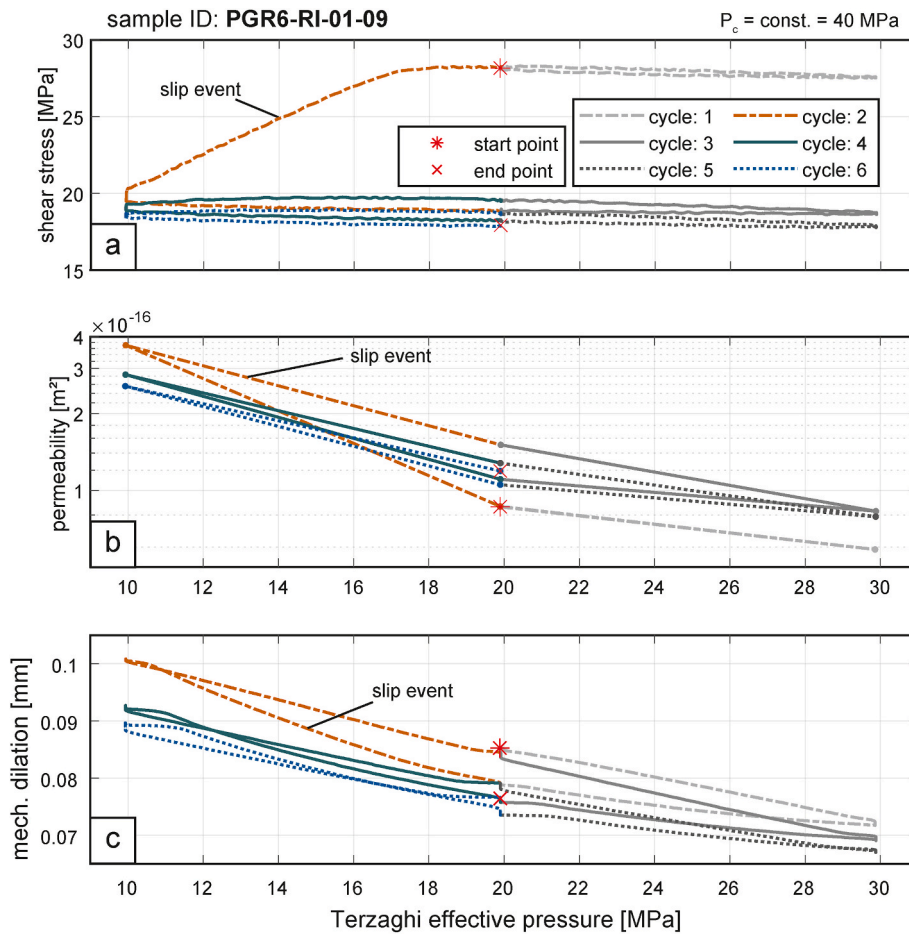


Fig. 8. Shear stress (a), permeability (b) and mechanical aperture (c) evolution during effective pressure changes of 10 MPa (sample PGR6-RI-01-09).

mm. The largest zone was zone III characterised by an inclined fracture orientation and consequent transension showing a highest mean aperture of 0.17 mm and a contact-area ratio of 31%.

Sample PGR6-RI-01-09 showed a similar distribution of zone I (transpression), zone II (simple shear) and zone III (transension). However, the mean apertures were overall higher (0.175 mm), with zone II showing the smallest mean aperture of 0.110 mm and highest

contact area-ratio of 41%. Furthermore, zone II was largest, meaning that the largest portion of the fracture was oriented vertically with simple shear features, and only small portions at the bottom show transensional features.

Comparing samples PGR6-RI-01-08 and PGR6-RI-01-09, the latter had an overall lower mean aperture and higher contact-area ratio with the largest portion showing simple shearing, while the other had a larger

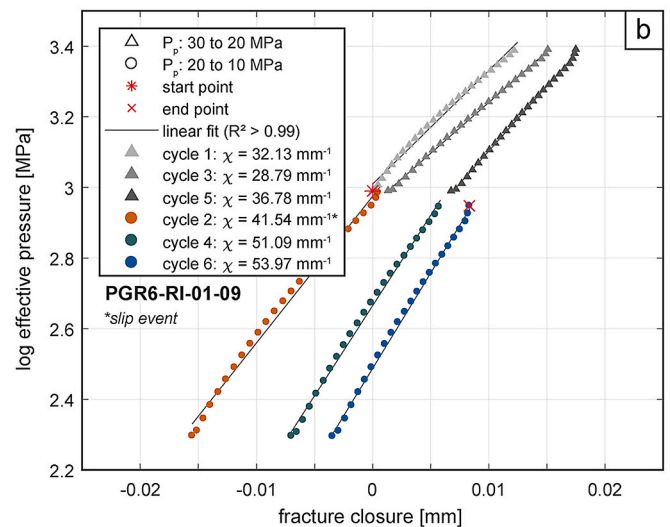
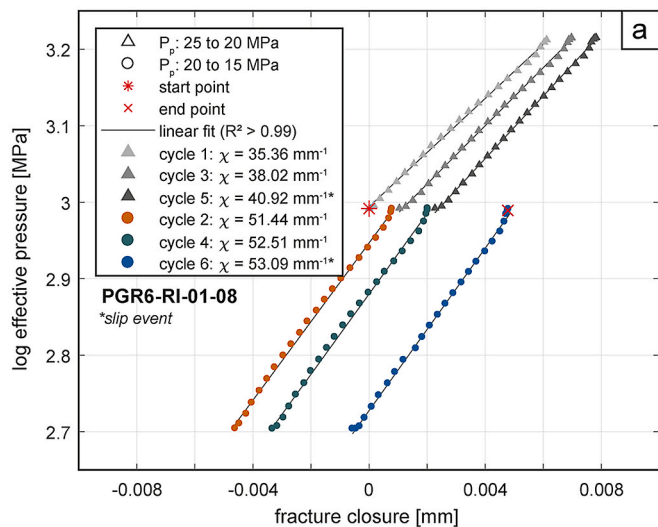


Fig. 9. Relative fracture closure vs. the logarithmic effective pressure change during the six effective pressure cycles (only pore pressure reduction) for sample PGR6-RI-01-08 (a) and sample PGR6-RI-01-09 (b).

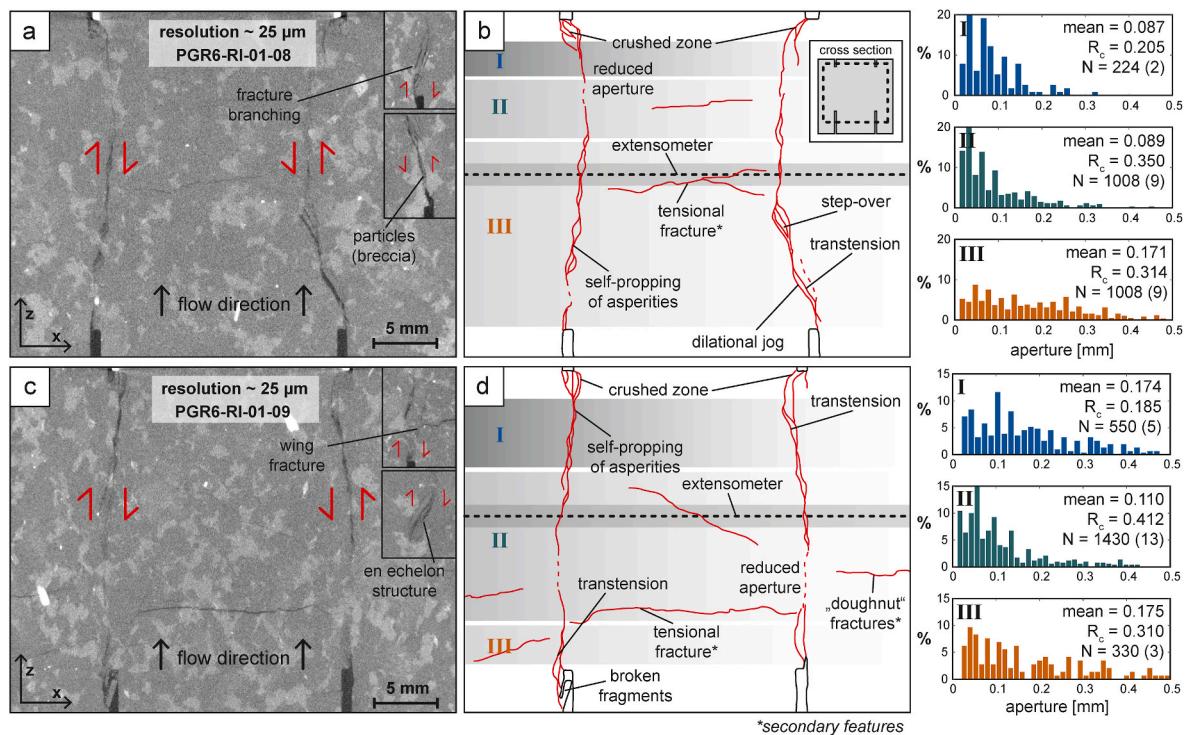


Fig. 10. Computed x-ray CT images and the reconstruction of the fracture system of sample PGR6-RI-01-08 (a, b) and sample PGR6-RI-01-09 (c, d).

Table 3
Experimental results.

| Sample ID | P_{eff} [MPa] | v_{prop} [mm/s] | K_{IIc} [MPa \cdot m $^{0.5}$] | k_{FOI} [-] | e_{mech} [mm] |
|---------------|-----------------|-------------------|-------------------------------------|---------------|------------------------------|
| PGR6-RI-01-07 | 20 | 0.1 | 16.42 | ~520 | – |
| PGR6-RI-01-08 | 20 | 0.3 | 15.71 | ~230 | 0.07 (0.09–0.1) ^a |
| PGR6-RI-01-09 | 20 | 0.3 | 15.34 | ~230 | 0.08 (0.07–0.1) ^a |

^a During pore pressure cycles, P_{eff} : effective pressure, v_{prop} : fracture propagation velocity, K_{IIc} : mode II fracture toughness, k_{FOI} : permeability fold of increase, e_{mech} : mechanical dilation after failure.

zone of transension with overall higher mean apertures and smaller contact area ratios. For both, shear zones cutting through feldspar minerals resulted in apertures of mostly zero while the largest open zones were found in quartz dominated areas. Fracture breccias or other fine and detached particles were found in every sample. The fact that they were located mostly in the bottom part of the fracture at the inflow zone indicates, that the particles were distributed and transported along the fracture, causing a further reduction in permeability.

Comparing the mechanical dilation (equation (5)) and volume-based dilation (equation (6.3)) with the aperture measured from the x-ray CT scan images, the post-testing CT images gave the largest mean aperture ranging from 0.09–0.18 mm while the mechanical dilation measured in-situ with extensometers gave 0.08–0.1 mm after failure.

4. Discussion

4.1. Microfault generation

Shear fracture geometries generated in conventional fracture permeability experiments sometimes do not represent the complex geometry of single fault zone on a laboratory scale. In this section, the fracture properties, the fracture geometry regarding structural features, as well as implications of the aperture distribution for the overall permeability and strength, obtained by the PTS test, will be discussed.

Our results suggest a sufficient reproducibility for this testing

procedure in terms of mode II fracture toughness, yield point, as well as permeability and dilation evolution. Monitoring the changes in inflow and outflow volume of the pore fluid during failure allows for a good control of the fracturing process and reveals similar processes as described by Backers,³⁷ where the fracture initiated from the outer bottom notch and propagated towards the inner top notch. However, it is not clear from the experiments whether wing fractures, as described by Backers,³⁷ cause the initial increase in inflow rate and that the actual shear fracture might form later and more rapidly at the point of failure. The fracture toughness values of about 15.3–16.4 MPa \cdot m $^{0.5}$ were slightly higher compared to other granites, for example Ävrö, Aue or Mizunami granite with values between 10.9–11.5 MPa \cdot m $^{0.5}$, tested under dry conditions.³⁵ While these experiments were performed at non-hydrostatic conditions, our experiments were performed with a confining stress acting on the top and bottom annulus of the sample. Furthermore, we were able to produce a single fracture at high effective pressures, which has been proven to be difficult in the past when applying mode II loading conditions in, for example, shear-box experiments.¹¹

We favour the term “microfault” for the structures produced in our experiments, although Crider⁴⁷ suggested differentiating between shear fractures (experimentally produced) and faults (field structures). The reason is, that most of the existing experimental studies applied the term “shear fracture” to describe tensile fractures with offset, which is not adequate. Although there is a discussion about whether fracture

initiation in PTS experiments is in shear mode,³⁴ the ongoing displacement of up to 1.2 mm clearly generated a principle shear plane with common features found in larger scale faults.^{48,49} The microfault geometry of the PTS test is rather complex and can be subdivided into three domains that are also found in natural fault systems: transpression, simple shear zones, transtension.^{50,51} The location of these systems along the fracture are assumed to control local permeability variation and depend on the fracture orientation, as well as on the degree of bending of the fault zone between top and bottom notch, and can also occur very locally. Transpression occurred mostly at the top of the sample, while transtension was found in the middle and lower section of the fracture zone. The fault zone structure is highly dependent on the stress and displacement magnitude, protolith and fluid flow.⁴⁹ A fine grained fault core (zone of reduced aperture), a fracture dominated damage zone and damage of linking damage structures⁴⁹ or “dilatational jogs”⁴⁸ were found in both our samples (Fig. 10). Detailed thin section analysis and a comparison with other rock types might provide more insights into the development of a fault zone, microfracture density or fault zone dimensions using the PTS test, to be able to compare this to general shear zone developments.⁵² In addition, the permeability can be adequately quantified due to the flow parallel orientation of fracture, meaning that compared to conventional tri-axial testing geometries, the fluid is not required to flow through a matrix before entering the fracture. Computed x-ray CT images also did show additional fractures such as radial fractures present in the matrix (Fig. 10). Due to the displacement and the interlocking of asperities the inner cylinder was pushing

against the outer cylinder, which resulted in brittle radial fracturing exclusively during unloading to atmospheric pressure at the end of the experiment (secondary feature). There was no indication of radial fracturing during displacement or pore pressure cycling since they would result in a larger permeability increase. Monitoring the electric conductivity of a silver paste applied to the circumference of the sample suggests an intact sample wall during fracture generation. To reduce the possibility of radial fracture generation, we recommend to increase the diameter of the sample while keeping the diameter of the notches. Furthermore, the top of the inner diameter needs support (steel ring) for hydrostatic pressure conditions, as hydrostatic conditions reduce the difference of compressional and tensile forces at the bottom notch, which are required to initiate shear fracture growth.³⁷ This possibly also explains the slightly higher load, or more precise, higher fracture toughness values, required for fracture generation.

4.2. Permeability and dilation evolution during fracturing and shearing

Quantifying and understanding the physical properties and processes that control the hydraulic-mechanical properties of fractured rocks are crucial for any engineering application in the subsurface. Experimental data of the generation and displacement of a single shear fracture zone under in-situ reservoir and fracture parallel flow conditions while measuring permeability are limited in the present literature. In the following, we will discuss our results of the permeability of microfaults framed in the context of existing approaches and outcomes in existing

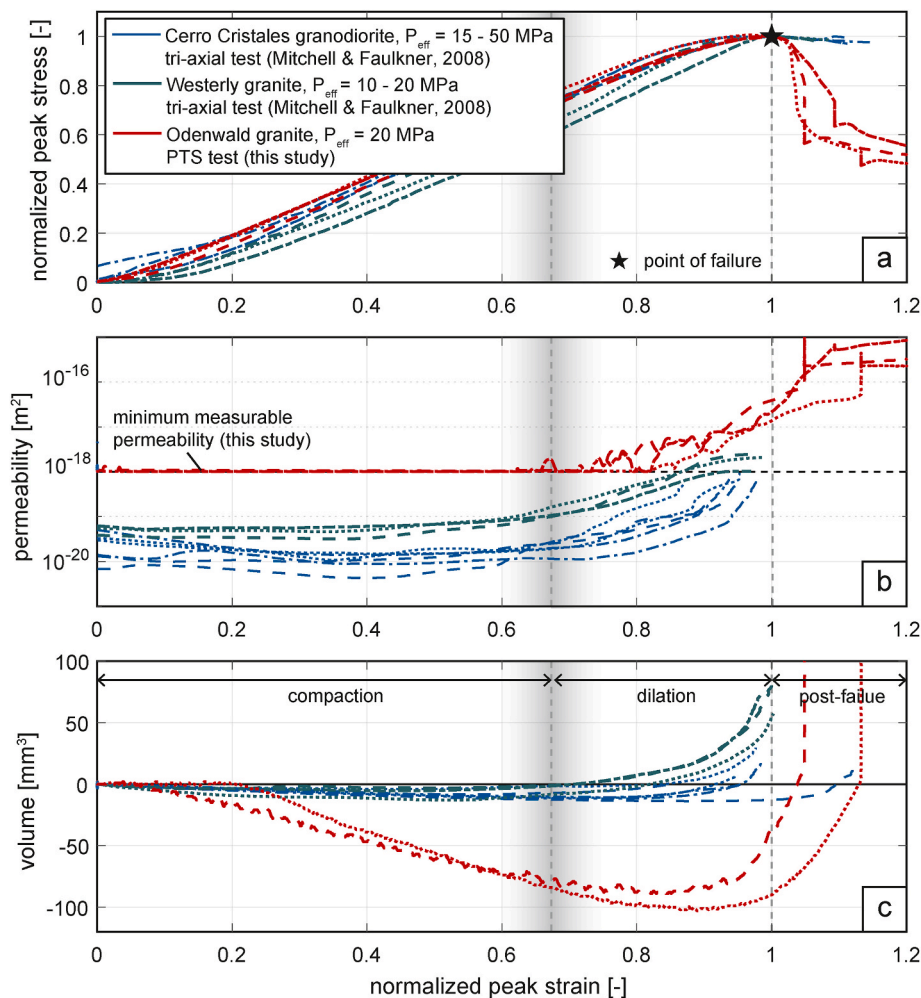


Fig. 11. Normalized stress-strain curves (a), permeability evolution (b) and volume changes (c) during failure for the Odenwald granite and the experiments with granite and granodiorite by Mitchell & Faulkner.²⁰

literature (Fig. 11).

In order to compare the measured permeability pre-, during and post-failure, the measured value should represent a pseudo steady-state value. To ensure these conditions we calculated the hydraulic diffusivity and the additional fluxes caused by the fracture formation. The diffusivity of $4.5 \cdot 10^{-6} \text{ m}^2/\text{s}$ was calculated according to Nicholas et al.,⁴³ resulting in a pore pressure diffusion to take less than 10 min. Furthermore, the generated fracture volume was measured to be maximum 0.2 ml within 90 min, while the applied flow rates varied between 0.4 ml/min and 1 ml/min. We concluded that both effects could be neglected for the permeability evolution during shearing, but consider the permeability during fracturing as transient.

Our results show that the magnitude of permeability enhancement is about 2 to almost 3 orders of magnitude, from less than 10^{-18} m^2 to more than 10^{-16} m^2 for a medium grained fresh granite such as the Odenwald granite with a sample diameter of 50 mm. This is more than the 17 to 35 times permeability increase reported by Ye & Ghassemi²⁸ on Sierra White Granite for their double flawed samples with a complex shear zone. However, it is similar to the experiments on Westerly granite and Cerro Cristales granodiorite by Mitchell & Faulkner²⁰ (Fig. 11b) using the pore pressure oscillation technique in conventional tri-axial testing at effective pressures of 10–50 MPa. Similar to their study, we assume that the damage in the surrounding rock matrix is negligible and that permeability is exclusively controlled by the generated microfault. The fracture volume evolution in the experiments by Mitchell and

Faulkner²⁰ shows a similar inflection at about 70–90% of the peak stress, although permeability increases already at lower strain, i.e. at about 60% of peak strain. The differences in fracture volume (Fig. 11c) arise from the sample and fracture geometry, or more precise, the fact that pore fluid can hardly travel through the rock matrix at the bottom and top of the sample in a tri-axial test, while there is an instant hydraulic connection and flow-parallel conditions in the PTS test. Generally, both results demonstrate that measuring permeability over more than three orders of magnitude experimentally during fracture initiation and propagation remains technically difficult. Still, similar to the experiments by De Paola et al.,¹⁶ the permeability evolution can be subdivided into three stages: compaction, dilation and post-failure, with the transition from compaction to dilation between 60 to 80% of peak strain. Assuming that Mitchell and Faulkner²⁰ rather measured pre-failure permeability evolution and that our results show the permeability increase during failure and at post-failure state, the total increase by brittle faulting can exceed 3 orders of magnitude (Fig. 10).

The bulk permeability of a fault is controlled by the size of the fault zone and the aperture resulting from shear dilation. The mechanical and volume based dilation, as well as fracture volume, are commonly used to determine the aperture changes in fractures due to changes in load,⁵ but present only bulk measurements for certain locations along the fracture. The x-ray CT images (Fig. 11) showed that local permeability is controlled by the distribution of aperture, which is again controlled by the fracture geometry and grain size. Similar to the study by Frash

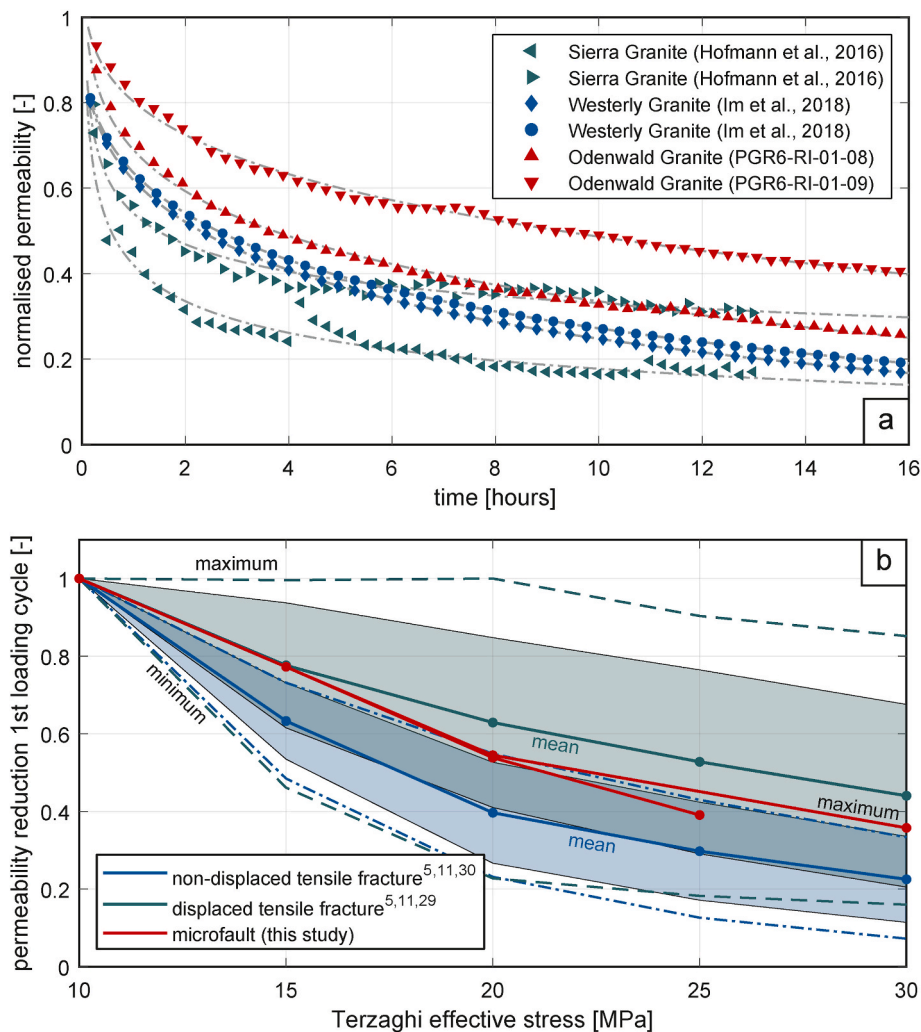


Fig. 12. Comparison of the permeability decay curves over time for different granites and fracture types reported from literature^{27,57} (a). Permeability reduction due to increasing effective pressure of non-displaced^{5,11,30} and displaced tensile fractures^{5,11,29} from literature and the microfaults from our study (b).

et al.,¹² aperture and therefore permeability are highly controlled by the presence of en-echelon or step-over structures, as well as fault particle transportation along the fault. Experimental studies with planar structures might simplify the processes involved,^{25–27} but do not reflect the evolution of permeability in active faults.

We demonstrated the ability to shear a fracture at an effective pressure of 20 MPa using the PTS test. Permeability increased by a factor of 1.1 to 4.0 by shearing under in-situ conditions right after producing the shear zone. Such an increase is comparable to experiments with sheared tensile fractures in other studies.^{21,24} A high dependence on the grain size is involved in the mechanical processes during shearing of a microfault, due to the sample size on a laboratory scale. The applied displacement did not exceed the grain size of the material and therefore no stick-slip behaviour, commonly observed in large scale fault mechanisms, was observed in our experiments. The realistic microfault geometry causes a heterogeneous aperture distribution, which highlights the importance of structural features, such as en-echelon or step-over structures, in faults during the displacement. We therefore also support the assumption that local pressure gradients play an critical role in controlling local permeability perturbations, when fluid is directly injected into a fault zone,⁵³ as well as when fluid is injected in an adjacent well.

4.3. Sustainability of permeability

The sustainability of the permeability of fault structures, in other words, the resistance of a fracture towards closing caused by pressure changes, is crucial for several underground applications. In the following chapter, we will discuss our results of longevity for microfault permeability and compare those with data from tensile and displaced tensile fractures published in literature (Fig. 12a and b).

Fault compaction due to elevated normal stress can significantly reduce the permeability of a microfault. Because of the relatively short testing period, we assume that no chemical rock-fluid interactions impact the hydraulic properties of the fracture. However, we could not consider possible particle redistribution affecting permeability. We therefore recommend to analyse the effluent in future studies. The observed reduction in permeability over time after shear fracture formation by a factor of 2.5 to 4 might be related to three possible mechanisms: (a) chemical rock-fluid interactions, i.e. dissolution or precipitation of minerals, (b) fines migration leading to a blockage of fluid pathways within the fault, and (c) mechanical creep, i.e. compaction or rearrangement of fault gouge particles. Mechanical back-slip is not possible, since the axial displacement piston was held in place after reaching a maximum of 1.2 mm.

Rock-fluid interactions, re-crystallizations or cementations are unlikely to influence permeability in our short-term experiments (several hours). Such processes evolve over long time-scales of several weeks³³ and require saline solution as the pore fluid while we used distilled water, such it is unlikely that this impacted permeability. For longer term experiments, such processes should be considered to impact fault permeability. Possible fines migration cannot be assessed in this study since it requires a microstructural analysis of the microfault. Comparing our data to literature data, the permeability decay curves over time are similar to those in literature^{5,27} for exponential or power law decay, although the normal effective stress range conditions (from 3 to 60 MPa) and fracture type (smooth saw-cut or displaced tensile type) differ to our study (Fig. 12a). Other authors suggest a linear decay⁵⁴ of permeability over several days, which did not fit our data. This might be caused by an insufficient resolution of permeability of the first 24 h in these tests. The main factor controlling the permeability decay cannot be explained by the data we obtained, but permeability losses up to one order of magnitude are possible within the first 16 h.

Considering pore pressure changes of ± 5 MPa to ± 10 MPa that simulate injection and production procedures in geothermal systems, permeability increased with decreasing effective pressure and decreased

by less than one order of magnitude. This process was rather reversible.

In Fig. 12b we compared our permeability during the effective pressure loading to fracture permeability data from literature for displaced and non-displaced tensile fractures. To be able to compare our sample permeability data, we need to calculate the fracture permeability, k_f , assuming that the permeability relates to the area of flow following Hofmann et al.⁵:

$$A_s k_s = A_m k_m + A_f k_f \quad (9.1)$$

where k is permeability, A is area of flow and the subscripts s, m, f relate to sample, matrix and fracture, respectively. The area of the sample is approximated by $A_s = \pi r^2$ and the fracture area is calculated from the circumference of the fracture multiplied by the aperture $A_f = a_h \pi (2r_{ID})^2$, with $2r_{ID} = r$. If we now assume that the matrix permeability of the granite is negligible ($k_m = 0$), we can rearrange equation (9.1) for the fracture permeability, which is given by the cubic law ($k_f = a^2/12$):

$$a^2 / 12 = (k_s \pi r^2) / (r \pi a_h) \quad (9.2)$$

This provides an equation for the hydraulic aperture similar to Hofmann et al.,⁵ but for a circular fracture:

$$a_h = \sqrt[3]{12 k_s r} \quad (9.3)$$

Inserting the hydraulic aperture, a_h , into the cubic law we obtain the fracture permeability ($k_f = a^2/12$), that we can now compare to the fracture permeability from the literature. The permeability reference value for normalisation at 10 MPa for our data is $1.97 \cdot 10^{-12} \text{ m}^2$. Comparing the permeability loss during the first loading cycle to other studies^{5,11,29,30} the permeability loss at the respective effective pressures are similar in magnitude with displaced fractures, during the first loading cycle when normalizing permeability to the permeability at 10 MPa effective pressure (Fig. 12b). Permeability loss at lower effective pressure is strongly affected by the experimental set up and is usually higher, such that those pressures are not considered here. Generally, displaced fractures and the microfaults in our study have a higher resistance to fracture closure compared to fractures without displacement. Higher displacements result in a higher sustainability of fracture permeability when comparing our results to those by Watanabe et al.¹¹ and Chen et al.²⁹ This implies, that the type of fracturing (matched tensile, displaced tensile or shear fracturing) is a key aspect when assessing the performance and sustainability of, for example, a geothermal reservoir. Moreover, all literature values presented here^{5,11,29,30} result from increasing confining pressure while in our experiments the pore pressure was decreased at constant confining pressure. In this context, we recommend to consider effective pressure coefficients^{31,55} instead of using Terzaghi's effective pressure. However, these coefficients are highly dependent on the rock type used and need to be determined experimentally.³¹ Changes in pore pressure, as in our experiments, are likely to have a smaller impact on fracture permeability, meaning that the change in permeability per step effective pressure is larger, assuming a coefficient of 0.9 for granite.⁵⁶ Considering several pressure cycles, the permanent permeability change in the presented experiments with six pressure cycles was an increase by a factor less than 1.4. Other studies suggested a reduction in permeability of up to one order of magnitude after two cycles, with the highest permeability damage during the first loading stage.⁵ We argue that the permeability of a microfault generated under in-situ conditions might be reversible due to the lack of plastic energy in the system. In experiments with displaced tensile fractures⁵ for example, the fracture preparation, i. e. placing two sample halves together by hand, causes a high amount of plastic energy. Under external load asperities break and the fracture re-arranges itself, causing a permanent permeability decrease in every loading cycle. This is not the case for in-situ fracture generation in the PTS test. Furthermore, aperture closure analysis suggests a stiffening of the fracture zone, i.e. less closure at similar stress,³² with an increasing

number of cycles, indicating compaction and stiffening effects during pressure cycling. The observed slip events when increasing the pore pressure lead to a minor permeability increase, as well as in a further stiffening of the fracture. Long-term permeability changes at high pressure and temperature of such small faults are required in the future to compare their behaviour to, for example, displaced tensile fractures.⁵⁴

5. Conclusions

Our experiments demonstrated an innovative technique to quantify the changes in permeability by introducing a shear fracture (microfault) in a previously intact rock sample simultaneous to fluid flow and at elevated effective pressure (pore and confining pressure). We modified the PTS setup by allowing for hydrostatic loading conditions, for the application of a controlled displacement after failure using a spring-supported core holder system, and for continuous fluid flow by introducing fluid ports to the end caps. A meaningful interpretation of the magnitude of fracture permeability change by introducing a realistic microscopic fault zone was therefore possible. Our results help to better understand and characterise the hydraulic and mechanical properties, as well as the sustainability of faulted reservoirs in general.

The following general conclusions can be drawn from our results: (1) the microfault geometry produced is rather complex but contains features that are commonly found in large scale fault zones, (2) the spatial distribution of aperture suggests a very local permeability distribution along the central shear zone, (3) permeability enhancement by brittle faulting in crystalline rock is about 2 to almost 3 orders of magnitude, while permeability increases at 60–80% of peak load, (4) shearing causes a slight increase in permeability by a factor of 1.1 to 4.0 which is possibly caused by the displacement magnitude being below grain size, (5) after compaction has ceased, which can cause reductions in permeability by a factor of 2.5 to 4, the generated microfault is hydraulically and mechanically sustainable when varying pore pressure by ± 5 to ± 10 MPa, (6) permeability is rather reversible and slight changes during pressure cycling are mainly caused by processes altering shear stress, (7) the resistance of a microfault to fracture closure at increasing effective pressure is in the range of displaced tensile fractures, and (8) the fracture types are a significant aspect when assessing the reservoir performance on a larger scale.

In the future, the dependence of fracture permeability on confining pressure and different rock types should be tested in order to quantify microfault permeability depending on rock type and rock physical properties. Additionally, acoustic emission monitoring would allow for better description on possible induced seismicity and permeability distribution of brittle fault zones in crystalline rock during effective pressure change.

Declaration of competing interest

The authors declare that they have no known competing financial interests or personal relationships that could have appeared to influence the work reported in this paper.

Acknowledgements

This project has received funding from the European Union's Horizon 2020 research and innovation programme under grant agreement No. 654662. We would also like to thank Ronny Giese for re-designing and realizing the PTS set up.

References

- Hofmann H, Zimmermann G, Zang A, Min KB. Cyclic soft stimulation (CSS): a new fluid injection protocol and traffic light system to mitigate seismic risks of hydraulic stimulation treatments. *Geoth Energy*. 2018;6(1). <https://doi.org/10.1186/s40517-018-0114-3>.
- McClure MW, Horne RN. An investigation of stimulation mechanisms in Enhanced Geothermal Systems. *Int J Rock Mech Min Sci*. 2014;72:242–260. <https://doi.org/10.1016/j.ijrmmms.2014.07.011>.
- Cuenot N, Charléty J, Dorbath L, Haessler H. Faulting mechanisms and stress regime at the European HDR site of Soultz-sous-Forêts. *France Geothermics*. 2006;35(5-6): 561–575. <https://doi.org/10.1016/j.geothermics.2006.11.007>.
- Evans KF, Genter A, Sausse J. Permeability creation and damage due to massive fluid injections into granite at 3.5 km at Soultz: 1. Borehole observations. *J Geophys Res Solid Earth*. 2005;110(4):1–19. <https://doi.org/10.1029/2004JB003168>.
- Hofmann H, Blöcher G, Milsch H, Babadagli T, Zimmermann G. Transmissivity of aligned and displaced tensile fractures in granitic rocks during cyclic loading. *Int J Rock Mech Min Sci*. 2016;87:69–84. <https://doi.org/10.1016/j.ijrmmms.2016.05.011>.
- Milsch H, Hofmann H, Blöcher G. An experimental and numerical evaluation of continuous fracture permeability measurements during effective pressure cycles. *Int J Rock Mech Min Sci*. 2016;89:109–115. <https://doi.org/10.1016/j.ijrmmms.2016.09.002>.
- Watanabe N, Hirano N, Tsuchiya N. Determination of aperture structure and fluid flow in a rock fracture by high-resolution numerical modeling on the basis of a flow-through experiment under confining pressure. *Water Resour Res*. 2008;44(6):1–11. <https://doi.org/10.1029/2006WR005411>.
- Fang Y, Elsworth D, Ishibashi T, Zhang F. Permeability evolution and frictional stability of fabricated fractures with specified roughness. *J Geophys Res Solid Earth*. 2018;123(11):9355–9375. <https://doi.org/10.1029/2018JB016215>.
- Vogler D, Amann F, Bayer P, Elsworth D. Permeability evolution in natural fractures subject to cyclic loading and gouge formation. *Rock Mech Rock Eng*. 2016;49(9): 3463–3479. <https://doi.org/10.1007/s00603-016-1022-0>.
- Develi K, Babadagli T. Experimental and visual analysis of single-phase flow through rough fracture replicas. *Int J Rock Mech Min Sci*. 2015;73:139–155. <https://doi.org/10.1016/j.ijrmmms.2014.11.002>.
- Watanabe N, Hirano N, Tsuchiya N. Diversity of channeling flow in heterogeneous aperture distribution inferred from integrated experimental-numerical analysis on flow through shear fracture in granite. *J Geophys Res Solid Earth*. 2009;114(4):1–17. <https://doi.org/10.1029/2008JB005959>.
- Frash LP, Carey JW, Welch NJ. Scalable en echelon shear-fracture aperture-roughness mechanism: theory, validation, and implications. *J Geophys Res Solid Earth*. 2019;124(1):957–977. <https://doi.org/10.1029/2018JB016525>.
- Ye Z, Ghassemi A. Injection-induced propagation and coalescence of preexisting fractures in granite under triaxial stress. *J Geophys Res Solid Earth*. 2019;124(8): 7806–7821. <https://doi.org/10.1029/2019JB017400>.
- Zhu W, Wong T. The transition from brittle faulting to cataclastic flow: permeability evolution. *J Geophys Res Solid Earth*. 1997;102(B2):3027–3041. <https://doi.org/10.1029/96jb03282>.
- Crawford BR. Experimental fault sealing: shear band permeability dependency on cataclastic fault gouge characteristics. *Geol Soc London Spec Publ*. 1998;127(1): 27–47. <https://doi.org/10.1144/gsl.sp.1998.127.01.04>.
- De Paola N, Faulkner DR, Colletini C. Brittle versus ductile deformation as the main control on the transport properties of low-porosity anhydrite rocks. *J Geophys Res Solid Earth*. 2009;114(6). <https://doi.org/10.1029/2008JB005967>.
- Elkhoury JE, Niemeijer A, Brodsky EE, Marone C. Laboratory observations of permeability enhancement by fluid pressure oscillation of in situ fractured rock. *J Geophys Res Solid Earth*. 2011;116(2):1–15. <https://doi.org/10.1029/2010JB007759>.
- Carey JW, Frash LP, Ickes T. Experimental investigation of shear fracture development and fluid flow in dolomite. In: ARMA, ed. *52 Nd US Rock Mechanics/ Geomechanics Symposium*. American Rock Mechanics Association; 2018. Seattle, Washington, USA, 17–20 June 2018.
- Shokouhi P, Jin J, Wood C, et al. Dynamic stressing of naturally fractured rocks: on the relation between transient changes in permeability and elastic wave velocity. *Geophys Res Lett*. 2020;47(1):1–10. <https://doi.org/10.1029/2019GL083557>.
- Mitchell TM, Faulkner DR. Experimental measurements of permeability evolution during triaxial compression of initially intact crystalline rocks and implications for fluid flow in fault zones. *J Geophys Res Solid Earth*. 2008;113(11):1–16. <https://doi.org/10.1029/2008JB005588>.
- Zhang Q, Li X, Bai B, Pei L, Shi L, Wang Y. Development of a direct-shear apparatus coupling with high pore pressure and elevated temperatures. *Rock Mech Rock Eng*. 2019. <https://doi.org/10.1007/s00603-019-1735-y>.
- Kluge C, Blöcher G, Milsch H, et al. Sustainability of fractured rock permeability under varying pressure. In: *Poromechanics 2017 - Proceedings of the 6th Biot Conference on Poromechanics*. 2017. <https://doi.org/10.1061/9780784480779.148>.
- Yeo IW, De Freitas MH, Zimmerman RW. Effect of shear displacement on the aperture and permeability of a rock fracture. *Int J Rock Mech Min Sci*. 1998;35(8): 1051–1070. [https://doi.org/10.1016/S0148-9062\(98\)00165-X](https://doi.org/10.1016/S0148-9062(98)00165-X).
- Lee HS, Cho TF. Hydraulic characteristics of rough fractures in linear flow under normal and shear load. *Rock Mech Rock Eng*. 2002;35(4):299–318. <https://doi.org/10.1007/s00603-002-0028-y>.
- Sheng M, Xu Z, Wang X, Li P. Experimental study on hydro-shearing propagation of an embedded fracture in hot dry granite rock. *GRC Trans*. 2018;42.
- Rutter EH, Mecklenburgh J. Hydraulic conductivity of bedding-parallel cracks in shale as a function of shear and normal stress. *Geol Soc London Spec Publ*. 2017;454(1):67–84. <https://doi.org/10.1144/sp454.9>.
- Im K, Elsworth D, Fang Y. The influence of pre-slip sealing on the permeability evolution of fractures and faults. *Geophys Res Lett*. 2018;45(1):166–175. <https://doi.org/10.1002/2017GL076216>.
- Ye Z, Ghassemi A. Injection-induced shear slip and permeability enhancement in granite fractures. *J Geophys Res Solid Earth*. 2018;123(10):9009–9032. <https://doi.org/10.1029/2018JB016045>.

- 29 Chen Z, Narayan SP, Yang Z, Rahman SS. An experimental investigation of hydraulic behaviour of fractures and joints in granitic rock. *Int J Rock Mech Min Sci.* 2000;37(7):1061–1071. [https://doi.org/10.1016/S1365-1609\(00\)00039-3](https://doi.org/10.1016/S1365-1609(00)00039-3).
- 30 Pyrak-Nolte LJ, Morris JP. Single fractures under normal stress: the relation between fracture specific stiffness and fluid flow. *Int J Rock Mech Min Sci.* 2000;37(1-2): 245–262. [https://doi.org/10.1016/S1365-1609\(99\)00104-5](https://doi.org/10.1016/S1365-1609(99)00104-5).
- 31 Walsh JB. Effect of pore pressure and confining pressure on fracture permeability. *Int J Rock Mech Min Sci.* 1981;18(5):429–435. [https://doi.org/10.1016/0148-9062\(81\)90006-1](https://doi.org/10.1016/0148-9062(81)90006-1).
- 32 Zangerl C, Evans KF, Eberhardt E, Loew S. Normal stiffness of fractures in granitic rock: a compilation of laboratory and in-situ experiments. *Int J Rock Mech Min Sci.* 2008;45(8):1500–1507. <https://doi.org/10.1016/j.ijrmmms.2008.02.001>.
- 33 Yasuhara H, Elsworth D. Compaction of a rock fracture moderated by competing roles of stress corrosion and pressure solution. *Pure Appl Geophys.* 2008;165(7): 1289–1306. <https://doi.org/10.1007/s00024-008-0356-2>.
- 34 Wu H, Kemeny J, Wu S. Experimental and numerical investigation of the punch-through shear test for mode II fracture toughness determination in rock. *Eng Fract Mech.* 2017. <https://doi.org/10.1016/j.engfracmech.2017.08.006>.
- 35 Backers T, Stephansson O. ISRM suggested method for the determination of mode II fracture toughness. *Rock Mech Rock Eng.* 2012;45(6):1011–1022. <https://doi.org/10.1007/s00603-012-0271-9>.
- 36 Meier T. The influence of temperature on mode II fracture toughness using the punch-through shear with confining pressure experiment. In: *71st EAGE Conf Exhib Inc SPE Eur 2009*. 2009:1–8. <https://doi.org/10.3997/2214-4609.201400344>. May.
- 37 Backers T. Fracture toughness determination and micromechanics of rock under mode I and mode II loading. *Univ Potsdam*. 2004;August:138.
- 38 Yoon J, Jeon S. Experimental verification of a pts mode II test for rock. *Int J Rock Mech Min Sci.* 2004. <https://doi.org/10.1016/j.ijrmmms.2004.03.012>.
- 39 Pei L, Blöcher G, Milsch H, et al. Thermal strain in a water-saturated limestone under hydrostatic and deviatoric stress states. *Tectonophysics.* 2016;688:49–64. <https://doi.org/10.1016/j.tecto.2016.09.020>.
- 40 Blöcher G, Kluge C, Goense T, Pei L, Bakker RR, Bruhn DF. Hydraulic-mechanical characterization of geothermal reservoir rocks. In: *European Geothermal Congress*. 2019. The Hague.
- 41 Darcy H. *Les Fontaines Publiques de La Ville de Dijon: Exposition et Application Des Principes a Suivre et Des Formules a Employer Dans Les Questions de Distribution d'eau*. 1856 <https://doi.org/10.1080/00150199208223391>.
- 42 Terzaghi K. *Erdbaumechanik Auf Bodenphysikalischer Grundlage*. Leipzig u. Wien: F. Deuticke; 1925.
- 43 Nicolas A, Blöcher G, Kluge C, et al. Pore pressure pulse migration in microcracked andesite recorded with fibre optic sensors. *Geomech Energy Environ.* 2020. <https://doi.org/10.1016/j.gete.2020.100183>.
- 44 Tan X, Konietzky H, Frühwirth T. Experimental and numerical study on evolution of biot's coefficient during failure process for brittle rocks. *Rock Mech Rock Eng.* 2015; 48(3):1289–1296. <https://doi.org/10.1007/s00603-014-0618-5>.
- 45 Barton N, Bandis S, Bakhtar K. Strength, deformation and conductivity coupling of rock joints. *Int J Rock Mech Min Sci.* 1985;22(3):121–140. [https://doi.org/10.1016/0148-9062\(85\)93227-9](https://doi.org/10.1016/0148-9062(85)93227-9).
- 46 Crawford BR, Tsenn MC, Homburg JM, Stehle RC, Freysteinson JA, Reese WC. Incorporating scale-dependent fracture stiffness for improved reservoir performance prediction. *Rock Mech Rock Eng.* 2017;50(12):3349–3359. <https://doi.org/10.1007/s00603-017-1314-z>.
- 47 Crider JG. The initiation of brittle faults in crystalline rock. *J Struct Geol.* 2015;77: 159–174. <https://doi.org/10.1016/j.jsg.2015.05.001>.
- 48 Peacock DCP, Nixon CW, Rotevatn A, Sanderson DJ, Zuluaga LF. Glossary of fault and other fracture networks. *J Struct Geol.* 2016;92:12–29. <https://doi.org/10.1016/j.jsg.2016.09.008>.
- 49 Faulkner DR, Jackson CAL, Lunn RJ, et al. A review of recent developments concerning the structure, mechanics and fluid flow properties of fault zones. *J Struct Geol.* 2010;32(11):1557–1575. <https://doi.org/10.1016/j.jsg.2010.06.009>.
- 50 Dewey JF, Holdsworth RE, Strachan RA. Transpression and transtension zones. *Geol Soc London Spec Publ.* 1998. <https://doi.org/10.1144/GSL.SP.1998.135.01.01>.
- 51 Jones RR, Tanner GPW. Strain partitioning in transpression zones. *J Struct Geol.* 1995;17(6):793–802. [https://doi.org/10.1016/0191-8141\(94\)00102-6](https://doi.org/10.1016/0191-8141(94)00102-6).
- 52 Cho N, Martin CD, Sego DC. Development of a shear zone in brittle rock subjected to direct shear. *Int J Rock Mech Min Sci.* 2008;45(8):1335–1346. <https://doi.org/10.1016/j.ijrmmms.2008.01.019>.
- 53 Passetlègue FX, Brantut N, Mitchell TM. Fault reactivation by fluid injection: controls from stress state and injection rate. *Geophys Res Lett.* 2018;45(23):12,837–12,846. <https://doi.org/10.1029/2018GL080470>.
- 54 Caulk RA, Ghazanfari E, Perdrial JN, Perdrial N. Experimental investigation of fracture aperture and permeability change within Enhanced Geothermal Systems. *Geothermics.* 2016;62:12–21. <https://doi.org/10.1016/j.geothermics.2016.02.003>.
- 55 Zoback MD, Byerlee JD. The effect of microcrack dilatancy on the permeability of westerly granite. *J Geophys Res.* 1975;80(5):752–755. <https://doi.org/10.1029/jb080i005p00752>.
- 56 Kranzz RL, Frankel AD, Engelder T, Scholz CH. The permeability of whole and jointed Barre Granite. *Int J Rock Mech Min Sci.* 1979;16(4):225–234. [https://doi.org/10.1016/0148-9062\(79\)91197-5](https://doi.org/10.1016/0148-9062(79)91197-5).
- 57 Ye Z, Ghassemi A. Experimental study on injection-induced fracture propagation and coalescence for EGS stimulation. *Proc 43rd Stanford Geotherm Work Reserv Eng Stanford Univ*; 2018:1–9. <https://pangea.stanford.edu/ERE/pdf/IGAstandard/SGW/2018/Ye.pdf>.